JOURNAL OF SPACECRAFT AND ROCKETS
Vol. 36, No. 2, March–April 1999

Base Flow Predictions for a Lightsat Launcher at Supersonic Speeds

M. Serpico,* A. Schettino,* and A. Ciucci†
Centro Italiano Ricerche Aerospaziali, 81043 Capua (CE), Italy
and
D. Falconi‡ and M. Fabrizi‡
Fiat Avio Comprensorio BPD, 00034 Colleferro (Rome), Italy

A numerical investigation of the base flowfield past a lightsat launcher under development in Italy is presented. The analysis regards different points along the flight path in the supersonic regime under axisymmetric conditions and has been focused on the base region of the missile with the aim to investigate the influence of different motor nozzle exit conditions (motor-on and motor-off) and different motor fluid properties (air/combustion products) on the base drag. This activity has been performed using both a Centro Italiano Ricerche Aerospaziali code and the RAMPANT commercial code. A general satisfactory agreement between the two codes is observed in the global aerodynamic coefficients; however, predicted local base pressures show some differences, probably due to the different turbulence models and different numerical methods employed. The numerical results indicate that, in the supersonic flight regime, the base region is only slightly affected by different fluids and motor conditions at the nozzle exit.

Nomenclature

C_D = drag coefficient
C_f = skin friction coefficient
MW = molecular weight
p = pressure, Pa
S = curvilinear coordinate, m
T = absolute temperature, K
v = velocity, m/s
x, y = coordinates, m
γ = ratio of specific heats
ρ = density, kg/m^3

Subscripts

b = base
ne = nozzle exit
∞ = freestream

Introduction

THE aerodynamic drag represents one of the most important parameters in the design of missile configurations. The base drag is usually one of the largest contributions to the total aerodynamic drag and is often very difficult to predict due to the complex flow phenomena occurring in the base region of the vehicle. The importance of base drag justifies the large efforts devoted to a correct prediction of the base flowfield.

Numerical methods for the aerodynamic prediction of missiles and launchers have grown from empirical methods and linearized and full potential methods, to Euler and boundary-layer methods, to full Navier–Stokes capabilities with turbulence modeling.[1–3] Today, the choice of the method will depend on the accuracy required and on the cost and effort constraints; simpler methods are often employed during the preliminary design phase, whereas more advanced computational fluid dynamics (CFD) tools are required in later phases of design, when unconventional configurations or complex flowfields are encountered and when the details of local flowfield properties are needed. Aerodynamic computations are used for flight performance estimates, aerodynamic coefficient predictions, and surface heat transfer and heat load calculations. Numerical techniques based on the full Navier–Stokes equations with turbulence modeling represent the state of the art for this kind of application. Turbulence models commonly used for industrial applications range from algebraic models, e.g., Baldwin–Lomax,[4,5] to two-equation models, e.g., κ–ϵ (Ref. 6). Turbulence modeling represents one of the major limitations in practical work and is still a major research subject, especially in highly compressible flows and separating flows.[7] Navier–Stokes methods, however, are computationally very intensive; therefore, their application to the field of launcher aerodynamics is still somewhat limited and requires the use of powerful computers to keep the run time to an acceptable level.

The work presented in this paper concerns a CFD analysis of the Italian lightsat launcher VEGA. VEGA is a family of launchers that is being developed to offer an optimized, low-cost solution of access to low Earth orbit for small satellites.[8] The VEGA family is currently composed of two launchers: the VEGA K0, devoted to lightweight (100–300-kg) small satellites, and the VEGA K for the medium-weight (up to 1000-kg) small satellites.

The aerodynamic analysis presented regards the VEGA K0 launcher. The K0 full configuration, shown in Fig. 1, has four stages. However, the launcher geometry considered, also shown in Fig. 1, is composed of three stages; the supersonic regime encountered after first-stage separation is the region of interest. In particular, activity has been focused on the numerical investigation of the base flow of the K0 launcher. The computations have been performed using advanced CFD codes, with the objective to investigate the influence that different nozzle flow properties and nozzle exit conditions have on the base drag for different supersonic Mach numbers.

Numerical Analysis

Numerical Codes

The computational investigation has been performed using two computer codes, briefly described in the following:

H2NS is a research code developed at Centro Italiano Ricerche Aerospaziali (CIRA) that solves the full Navier–Stokes equations on structured grids for both internal and external flows, for two-dimensional or axisymmetric geometries, with chemical and vibrational nonequilibrium. A finite volume technique is adopted, with a flux difference splitting Riemann solver formulation[9,10] with

Received Aug. 30, 1997; revision received April 8, 1998; accepted for publication Nov. 9, 1998.

*Research Engineer, Aerothermodynamics Section, Via Maiorise.
†Senior Engineer and Head, Propulsion Section, Corso Garibaldi 22. Member AIAA.
‡Aerospace Engineer, Thermofluidynamics Section, Corso Garibaldi 22. Member AIAA.

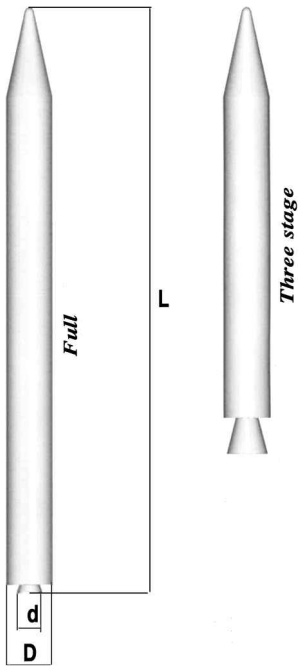

Fig. 1 VEGA K0 launcher configurations. Full configuration: L = 19.560 m, d = 1.024 m, and D = 1.908 m; and three-stage configuration: L = 14.944 m, d = 1.674 m, and D = 1.908 m.

a second-order essentially nonoscillatory (ENO) reconstruction of fluxes at cell interfaces. A detailed description of this solver is given in Refs. 11–13, in which the code has been extensively tested and validated by computing different flowfields, such as hyperboloid flare, blunt-body, and control surface geometries. Different thermochemical nonequilibrium and transport models are available in the code. In the hypothesis of perfect gas, the laminar viscosity is calculated by means of the Sutherland law. Turbulence effects are accounted for by modeling the eddy viscosity through an algebraic turbulence model.[14]

RAMPANT is a commercial code that solves the full three-dimensional Navier–Stokes equations in complex geometries.[15] It uses unstructured meshes with triangular elements in two dimensions and tetrahedral elements in three dimensions. The code implements a standard κ–ϵ turbulence model and a Renormalization Group (RNG) two-equation model. This code has been largely used to predict different flowfields, including aerospace, turbomachinery, automobile, and heat exchanger problems. Release 3.1 has been employed, under licence, in this study.

Method of Solution

Numerical investigations of the flowfield have been carried out for three points along the flight path, corresponding to freestream Mach numbers of 1.2, 3, and 6, respectively. As already indicated, the numerical study has been focused on the base region of the launcher. Both the base flow without an exhaust jet (motor-off) and the afterbody flowfield when the nozzle plume is present (motor-on) have been computed using both H2NS and RAMPANT codes. Furthermore, an investigation of the changes in the base flow patterns with different flow properties of the nozzle exhaust plume has been conducted with the H2NS code only. All computations have been performed using a Silicon Graphics Power Challenge parallel machine. The flowfield has been assumed axisymmetric and turbulent. A somewhat different solution strategy has been followed for each of the two codes.

H2NS Strategy

A flowfield segmentation procedure has been adopted with the H2NS code. This approach has been also followed by Sahu.[16] Even though the code can compute the full flowfield, including the base region, for supersonic flows a solution can be obtained more efficiently by splitting the computation into a forebody domain and an

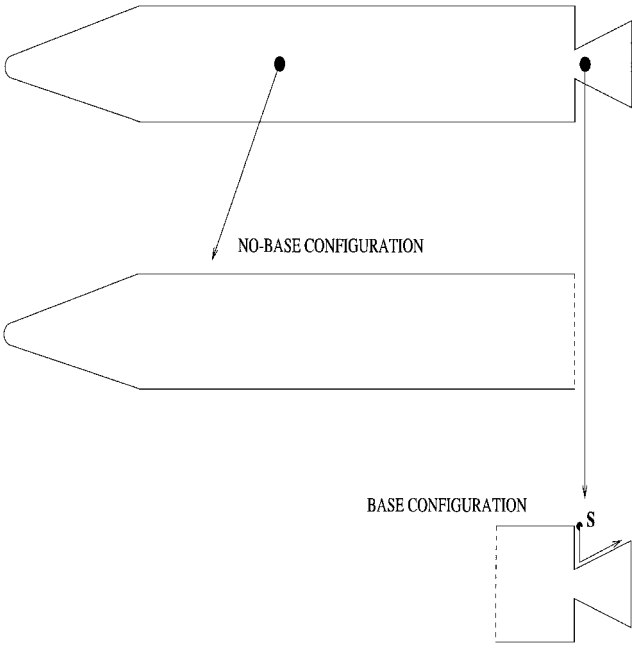

Fig. 2 VEGA K0 configurations used for the numerical simulations.

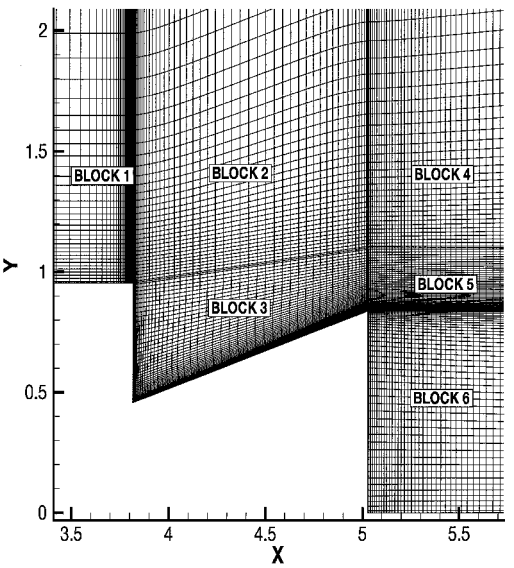

Fig. 3 Close-up of the grid used for the H2NS base flow computations.

afterbody domain. The former concerns the entire launcher up to the sharp corner at the base and is referred to as the *no-base configuration*; this configuration consists of a spherical nose tangent to a cone followed by a cylindrical body. The latter (afterbody domain) includes the base region of the launcher with the motor nozzle and starts at a station located 2.0 launcher diameters upstream of the base corner; this is referred to as the *base configuration.* These configurations are schematically shown in Fig. 2. The no-base solution provides the upstream boundary condition for the computation of the flowfield of the base configuration. This technique is computationally more efficient than calculating the full flowfield in a single sweep and allows a better refinement of the grid in the base region; furthermore, motor-off and motor-on solutions can be obtained without repeating the no-base computations.

The computational grid used for the no-base computations is of the C type and has about 14,000 grid points; the grid adopted for the base configuration has six blocks containing approximately 17,000 nodes, about 2000 of which are clustered at the base and nozzle walls. Figure 3 shows a close-up view of the base grid. To determine grid dependency on the flow solution in the base region, computations were made, increasing the number of points clustered

Table 1 Grid dependency analysis (Mach = 6)

	$C_{D_{\text{pressure}}}$	
Base grid	Wall base	Wall nozzle
Coarse (2000 pt.)	$1.731E-2$	$-4.346E-3$
Fine (4000 pt.)	$1.724E-2$	$-4.369E-3$

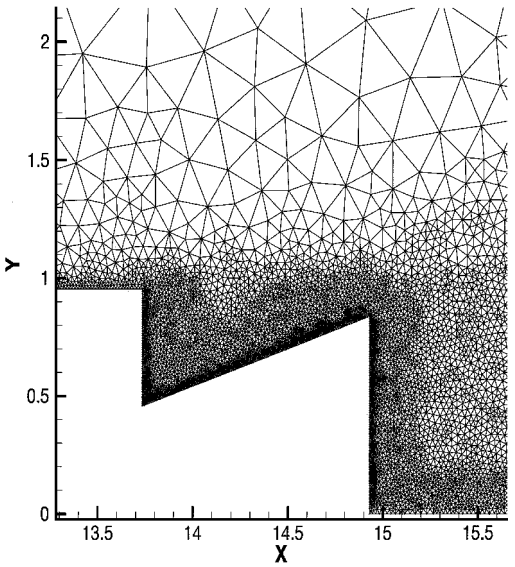

Fig. 4 RAMPANT grid: close-up of the base region.

at the base walls (block 3) up to around 4000. The solutions indicate that grid independency already is achieved with the initial grid; the very small change in base drag coefficient is reported in Table 1. The CPU time varied significantly depending on the run conditions, ranging from 20 to 45 h.

The turbulence model employed in the H2NS code is the algebraic model of Baldwin and Lomax. This turbulence model has been applied by many researchers for the solution of this type of flow.[4,17,18] To correctly employ the Baldwin–Lomax algebraic turbulence model, a reference wall within the computational domain is needed. For the near-wake region of the base configuration, following the work of Sahu,[19,20] the motor centerline has been chosen as the reference line.

RAMPANT Strategy

A somewhat different approach was adopted with the RAMPANT code. Because of the unstructured method employed in RAMPANT, domain segmentation was not easily applicable; therefore, the full flowfield, including the base region, was computed in a single run. The geometry considered for these runs is shown in Fig. 2. The computational grid used for all runs has approximately 35,000 grid points, with about 4000 nodes placed within the base region of the flow. The number of grid points located in this region is considerably higher than the number of nodes in the same region with the H2NS structured grid; this is due to the lower grid control of the unstructured mesh. A close-up view of the RAMPANT unstructured grid in the base region is shown in Fig. 4. Preliminary runs have shown that grid independency on the flow solution in the base region is attained with this grid. The CPU time required for the RAMPANT computations is about 25 h.

The turbulence model selected for all RAMPANT computations was a standard $\kappa-\epsilon$ two-equation model, which is the second most significant difference between the two solution strategies adopted.

Initial and Boundary Conditions

The inflow conditions used in the present numerical study have been supplied by Fiat Avio Comprensorio BPD and are reported in Ref. 21. The freestream boundary conditions are summarized in Table 2.

Table 2 Inlet boundary conditions

Test case	Mach number	ρ_∞, kg/m^3	p_∞, Pa	Reynolds number, 1/m
I	1.2	0.3181	19,782	$7.9194E+06$
II	3.0	0.0633	3,973	$3.9276E+06$
III	6.0	0.0012	94.0	$0.1393E+06$

Table 3 Inlet conditions at nozzle exit section

Test case	p_{ne}, Pa	v_{ne}, m/s	T_{ne}, K	γ	MW
I	16,330	2,807	1,316	1.1998	27.660
II	17,170	2,808	1,318	1.1997	27.672
III	11,440	2,799	1,300	1.2009	27.577

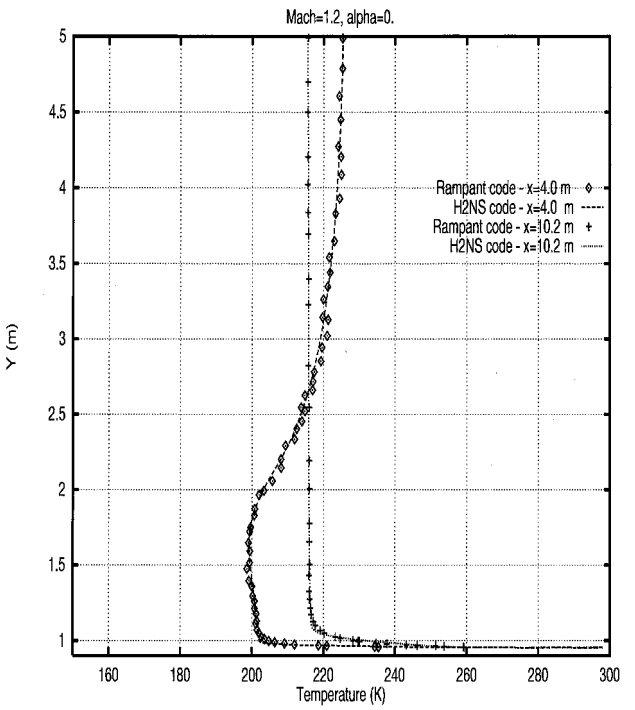

Fig. 5 Comparison of temperature profiles at x = 4.0 and 10.2 m; Mach = 1.2.

For the motor-on cases, the inflow boundary conditions are given in Table 3, in which pressure, velocity, temperature, ratio of specific heats, and molecular weight are specified. These conditions correspond to an exit Mach number of about 4.1 and pressure ratios p_{ne}/p_∞ of 0.825, 4.332, and 121.70 for tests I, II, and III, respectively. These conditions refer to the motor combustion gases. For the simulations with air, the same mass flow rate, pressure, and temperature at nozzle exit have been assumed.

The solution of the no-base flowfield provides the inflow boundary condition to be assigned on the left-hand side of block 1 for the H2NS runs. For the RAMPANT computations, a freestream turbulence intensity of 1% was chosen; for the motor-on cases, the turbulence intensity at the nozzle exit was fixed at the level of 20%, which is a typical value encountered in similar motor nozzles. A symmetry boundary condition is used at the centerline (axis). At the outflow boundary, the flow variables are simply extrapolated from the known inner values. A no-slip boundary condition is imposed on the launcher walls, including the boundary representing the nozzle exit area in the motor-off cases, and the wall temperature is set equal to 273 K. In all computations the outer boundary was set at a distance of three launcher lengths. For the base computations the downstream boundary was set at a distance of two launcher lengths from the nozzle exit.

All computations have been started from a uniform initialization of the flow variables at their freestream values. The motor-on cases, on the other hand, have been started from the relevant

motor-off case by changing the boundary conditions at the nozzle exit patch.

Discussion of Results

To ensure that the base flow is computed under similar conditions with the two codes, a preliminary analysis of the flowfield upstream of the base region, obtained with the H2NS no-base computations and with the RAMPANT full computations, has been conducted. Then a detailed analysis of the base flowfield was performed, with particular attention to the influence on the base drag produced by a different gas at the nozzle exit and by different motor conditions. The code-to-code comparison has considered both local quantity profiles and global aerodynamic coefficients on the cylindrical section of the launcher and in the base region under both motor-on and motor-off conditions.

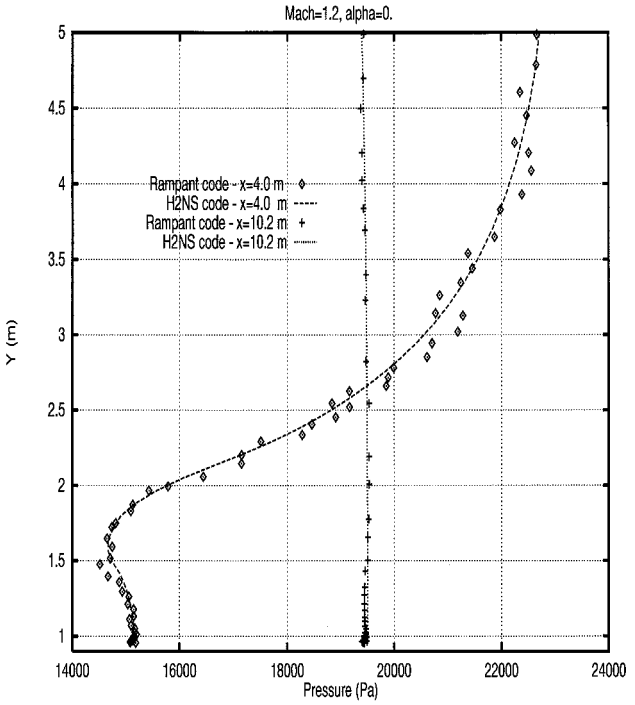

Fig. 6 Comparison of pressure profiles at x = 4.0 and 10.2 m; Mach = 1.2.

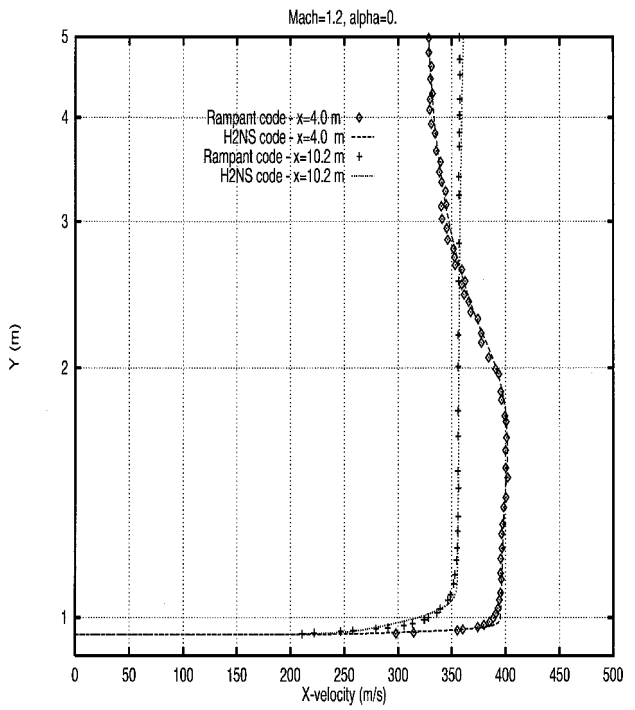

Fig. 7 Comparison of x-velocity profiles at x = 4.0 and 10.2 m; Mach = 1.2.

No-Base Configuration

The comparisons of the temperature, pressure, and axial velocity profiles at two different stations along the cylindrical part of the launcher, obtained with the H2NS and RAMPANT codes, are shown in Figs. 5–7 for the Mach = 1.2 test case and in Figs. 8–10 for the Mach = 6.0 test case. The two axial stations are taken at 4 and 10.2 m from the launcher nose, respectively; the station at $x = 10.2$ m represents the inflow boundary of the base configuration computational domain, whereas station $x = 4$ m is approximately at the beginning of the cylindrical section of the launcher. The Mach = 6 case has a lower Reynolds number with respect to the Mach = 1.2 case, which justifies the larger boundary layer; the shock wave, being closer to the body at higher Mach numbers, is clearly captured in Figs. 8–10. The comparison shows a satisfactory agreement of results for the Mach = 1.2 case, whereas some differences are observed in the

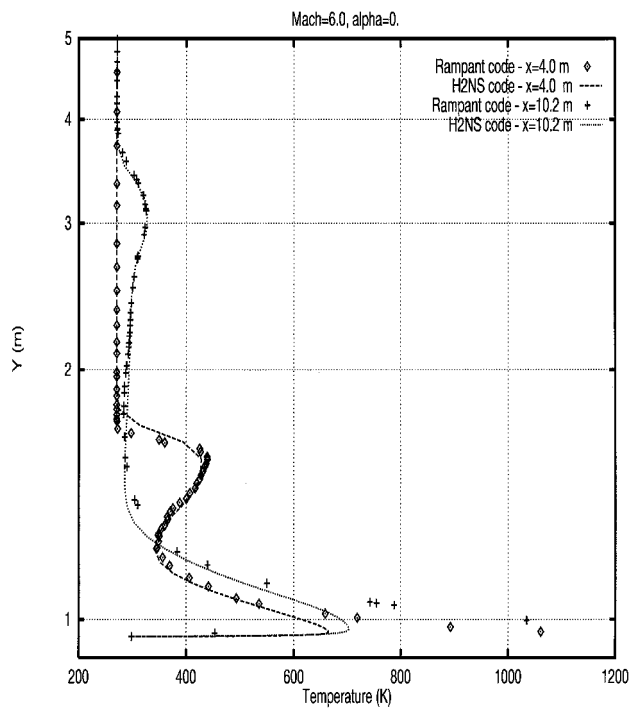

Fig. 8 Comparison of temperature profiles at x = 4.0 and 10.2 m; Mach = 6.0.

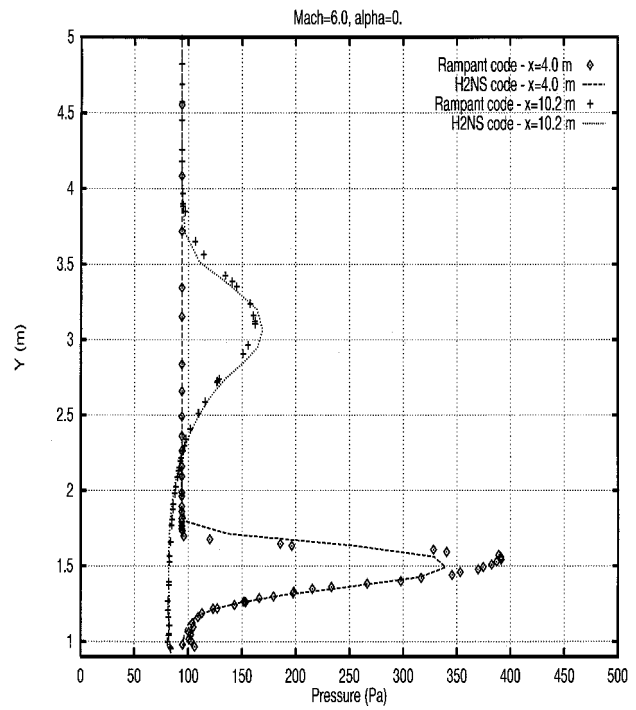

Fig. 9 Comparison of pressure profiles at x = 4.0 and 10.2 m; Mach = 6.0.

Mach = 6.0 run. In particular, the temperature and pressure peaks computed with the RAMPANT code are larger with respect to the values given by the H2NS code. These differences may be partially due to the different turbulence models used in the two codes.

The comparison of the drag coefficients (the pressure contribution, the viscous contribution, and their sum) for the no-base configuration (sphere, cone, and cylinder) is reported in Tables 4–6, where the percent differences between the drag coefficients computed with the two different codes are reported in the last row $\{\Delta\% = 100[(\text{RAMPANT} - \text{H2NS})/\text{H2NS}]\}$.

As shown Tables 4–6, satisfactory agreement exists between the two codes. The largest differences arise on the viscous drag coefficient, which, however, gives only a small contribution to the total drag; the highest percent difference occurs in $C_{D_{\text{viscous}}}$ at the Mach number of 6, in agreement with the discrepancies observed in the given profiles. Again, this is attributed to the different turbulence models.

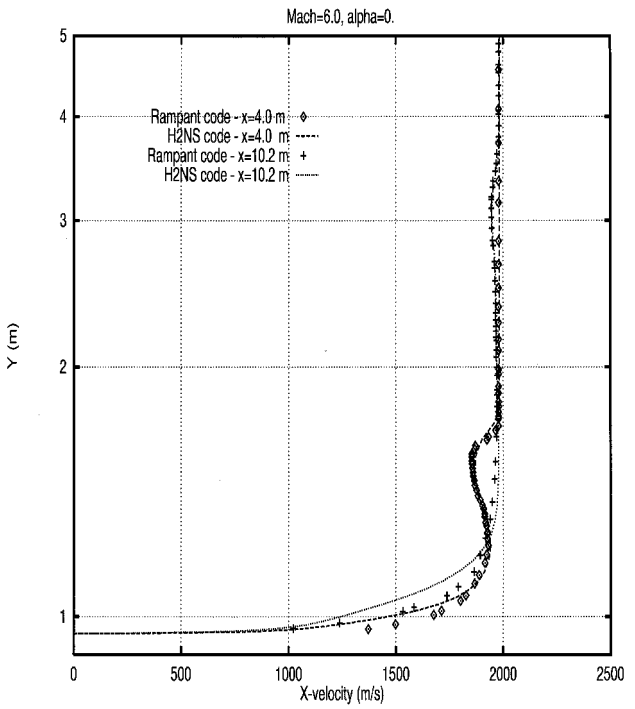

Fig. 10 Comparison of x-velocity profiles at x = 4.0 and 10.2 m; Mach = 6.0.

Base Configuration

The results obtained on the no-base configuration have been used as input data for the different H2NS base flow calculations.

To assess the influence of the turbulence model and/or computational method on the solution, a comparison between the results obtained with the RAMPANT and H2NS codes has been carried out. The pressure distributions on the launcher base are shown in Fig. 11 for Mach = 1.2 under motor-off conditions, the Mach = 3 with motor-on, and Mach = 6.0 with motor-off. The comparison between the base drag coefficient for the RAMPANT and H2NS results is shown in Table 7, where the percent difference between the two results is reported in the last row $\{\Delta\% = 100[(\text{RAMPANT} - \text{H2NS})/\text{H2NS}]\}$.

The results show that as the Mach number increases the base pressure becomes progressively lower with respect to the freestream pressure. However, the base drag coefficient tends to decrease due to the higher flow velocity. Rather good agreement is observed between

Table 4 Drag coefficient comparison: Mach = 1.2

Solver	$C_{D_{\text{pressure}}}$	$C_{D_{\text{viscous}}}$	$C_{D_{\text{total}}}$
RAMPANT	0.3103	$4.758E-2$	0.3579
H2NS	0.3050	$4.524E-2$	0.3502
$\Delta\%$	1.74	5.17	2.20

Table 5 Drag coefficient comparison: Mach = 3.0

Solver	$C_{D_{\text{pressure}}}$	$C_{D_{\text{viscous}}}$	$C_{D_{\text{total}}}$
RAMPANT	0.1918	$4.155E-2$	0.2333
H2NS	0.1893	$3.930E-2$	0.2286
$\Delta\%$	1.32	5.72	2.06

Table 6 Drag coefficient comparison: Mach = 6.0

Solver	$C_{D_{\text{pressure}}}$	$C_{D_{\text{viscous}}}$	$C_{D_{\text{total}}}$
RAMPANT	0.1750	0.0594	0.2345
H2NS	0.1664	0.0669	0.2333
$\Delta\%$	5.16	−11.2	0.52

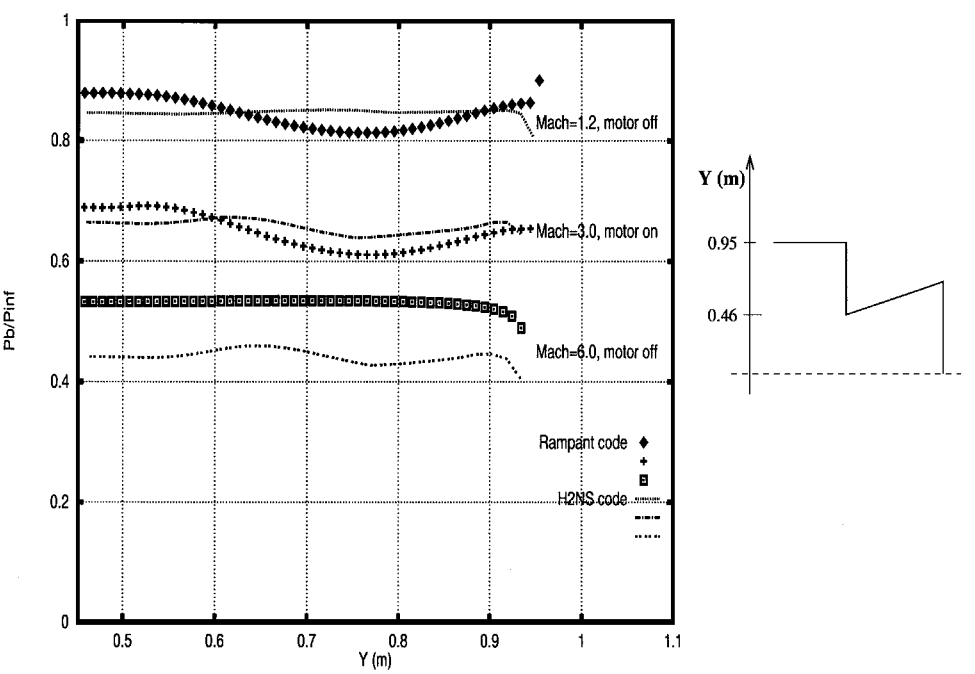

Fig. 11 Base wall pressure for RAMPANT and H2NS computations.

Table 7 Comparison of base drag coefficients

Solver	Mach = 1.2, motor-off	Mach = 3.0, motor-on	Mach = 6.0, motor-off
RAMPANT	0.1070	0.0431	0.0140
H2NS	0.1170	0.0415	0.0170
$\Delta\%$	8.55	3.85	−17.65

Table 8 Motor-on and motor-off base drag coefficients

	Freestream Mach number		
Nozzle exit	1.2	3.0	6.0
Motor-on	0.113	0.0415	0.0173
Motor-off	0.117	0.0469	0.0170
$\Delta\%$	−3.42	−11.51	1.76

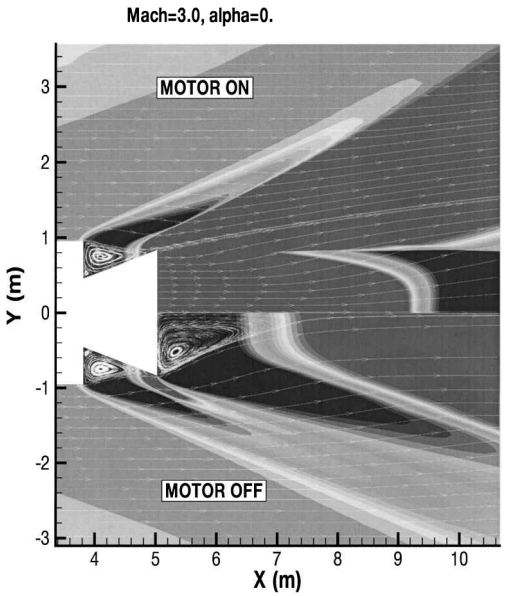

Fig. 12 Comparison of streamlines and pressure fields for motor-on and motor-off conditions.

the base pressure levels predicted with the two codes, except for the Mach = 6 case, in which the RAMPANT values are about 20% higher than those calculated with the H2NS code. The base drag decreases with respect to the total no-base drag at higher Mach numbers, ranging from about 33.4% at Mach = 1.2 to 20.5% at Mach = 3 and to 7.4% at Mach = 6. Thus, the largest differences occur when the base drag contribution is lowest.

This discrepancy in base pressure levels predicted with the two codes is probably a consequence of the difference between the algebraic turbulence model and the κ–ϵ model. Some effects on the solution may be due also to the different numerical approaches of the two codes, especially the use of a structured grid in one case and of an unstructured grid in the other case. Better prediction capabilities of the κ–ϵ model have been documented for a cylindrical afterbody without base bleed and with base bleed at moderate exhaust velocities.[19,20] No experimental results are available for comparison at this time for the geometry considered in this work. Therefore, no definite conclusions on the accuracy of the base pressure predictions can be drawn.

The influence that different motor conditions at the nozzle exit (motor-on/motor-off, air/combustion gases) have on the base flowfield patterns has been investigated by means of the H2NS code. The different structure of the flow for motor-on and motor-off at Mach = 3 is shown in Fig. 12, where the pressure contours are shown together with some streamlines. The large recirculation behind the nozzle exit section obviously disappears when the plume is present. However, this seems to have a small effect on the flow characteristics within the base region, which presents a main recirculation with a reattachment point located toward the end of the nozzle wall and a small secondary recirculation at the base-nozzle corner. The comparison of the aerodynamic base drag coefficients is reported in Table 8 for the different Mach numbers $\{\Delta\% = 100[(\text{motor-on} - \text{motor-off})/\text{motor-off}]\}$.

The effect of the nozzle exhaust fluid properties has been assessed simulating combustion products instead of air. A comparison of Mach contours at Mach = 6 is shown in Fig. 13. Significant differences are observed within the exhaust plume, but only slight effects are felt upstream in the base region, where the recirculation shape does not change appreciably. The base drag coefficients for air and combustion gases are reported in Table 9 for comparison $\{\Delta\% = 100[(\text{air} - \text{combustion gases})/\text{air}]\}$.

The pressure distributions on the base wall and on the nozzle wall are shown in Figs. 14–16 for the Mach numbers of 1.2, 3, and 6, respectively. The pressure is plotted vs the curvilinear coordinate S, with the origin at the base upper corner and running as shown in Fig. 2. The results for motor-off and motor-on with air or combustion

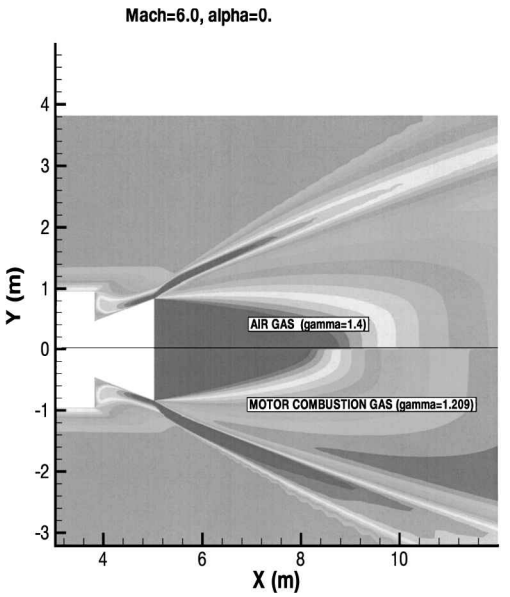

Fig. 13 Comparison of Mach number fields for motor-on with different fluid properties at the nozzle exit.

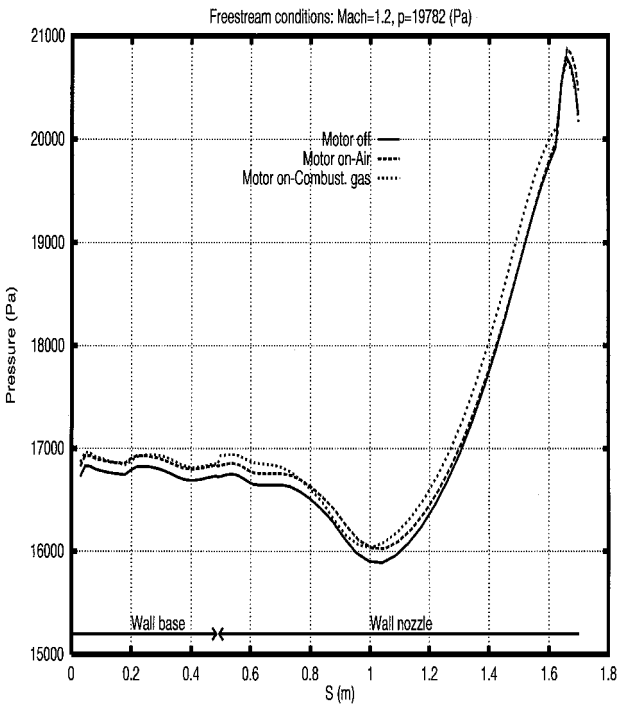

Fig. 14 Comparison of pressure distributions on the base and nozzle walls for motor-off and motor-on conditions; Mach = 1.2 and p = 19,782 Pa.

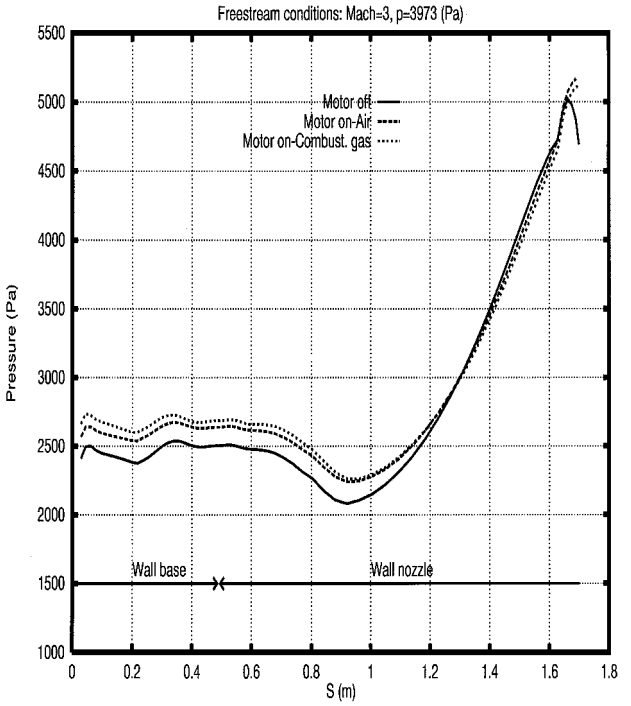

Fig. 15 Comparison of pressure distributions on the base and nozzle walls for motor-off and motor-on conditions; Mach = 3 and $p = 3973$ Pa.

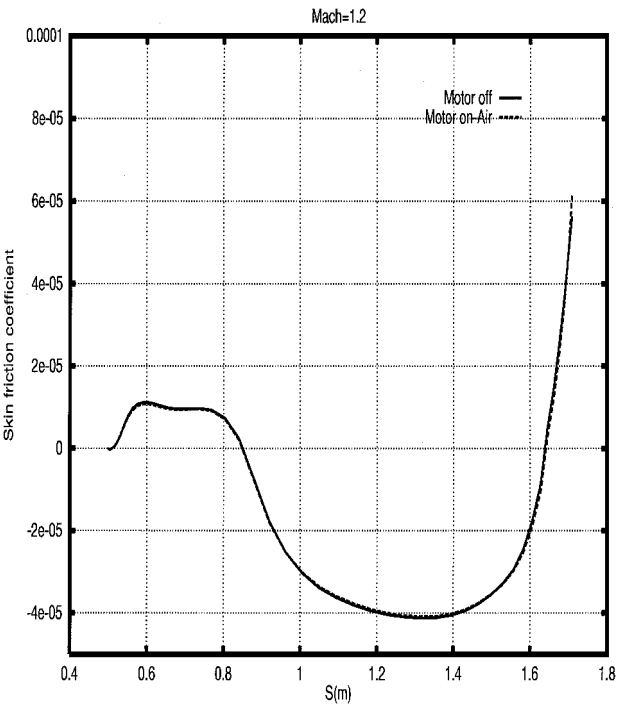

Fig. 17 Comparison of the skin-friction coefficient distributions on the nozzle wall for motor-off and motor-on conditions; Mach = 1.2.

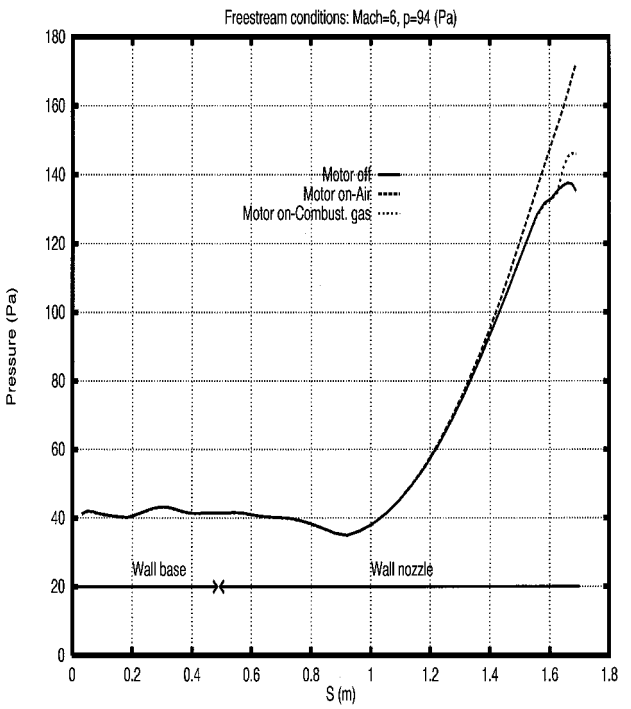

Fig. 16 Comparison of pressure distributions on the base and nozzle walls for motor-off and motor-on conditions; Mach = 6 and $p = 94$ Pa.

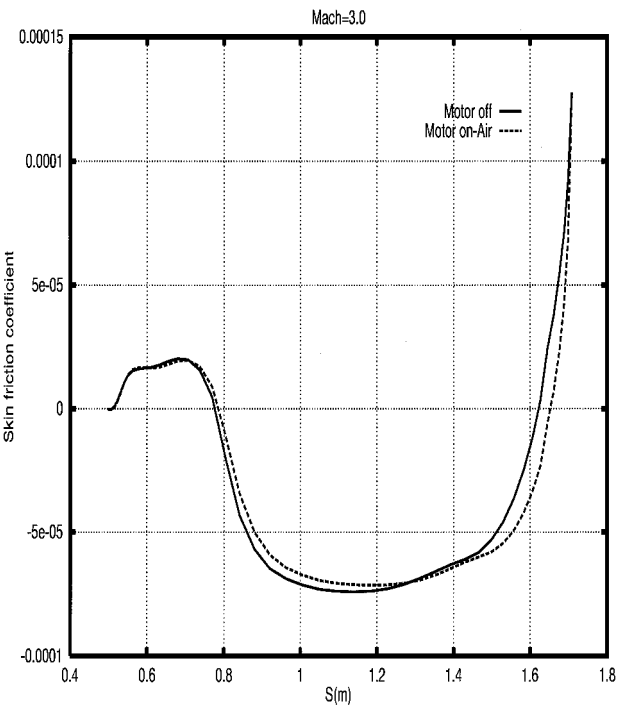

Fig. 18 Comparison of the skin-friction coefficient distributions on the nozzle wall for motor-off and motor-on conditions; Mach = 3.0.

gases are reported. Small differences are observed among the three curves for all Mach numbers, which confirms that the conditions at the nozzle exit do not significantly affect the base flow structure and ultimately the base drag.

Finally, the distributions of the skin-friction coefficients along the nozzle outer wall for motor-off and motor-on (using air) are shown in Figs. 17–19 for the three Mach numbers under consideration. Again, the curvilinear abscissa S has been used for convenience. The positions of the main reattachment point and of the separation point between primary and secondary recirculations are clearly shown by the points at which $C_f = 0$. The skin-friction coefficient starts with a positive value, being the axial velocity component of the same sign with respect to the reference velocity (in the positive axial direction); then with increasing S it becomes negative in the central part and positive again after crossing the main reattachment point. It is interesting to note that, as the Mach number increases, the location of the main reattachment point tends to move closer to the base under motor-off operation, probably because of the stronger expansion at the base top corner. On the contrary, when the motor is on, the exhaust plume has a suction effect on this reattachment point, which is shifted toward the nozzle exit tip.

The results obtained in this work show that, for a base geometry including an exhaust nozzle, for supersonic freestream Mach numbers, the base drag is only slightly affected by the nozzle exit conditions when the main reattachment point is located on the nozzle outer wall.

Table 9 Base drag coefficients for different fluid properties

	Freestream Mach number		
Gas at nozzle exit	1.2	3.0	6.0
Air	0.113	0.0415	0.0173
Combustion gases	0.109	0.0395	0.0170
$\Delta\%$	3.54	4.82	1.73

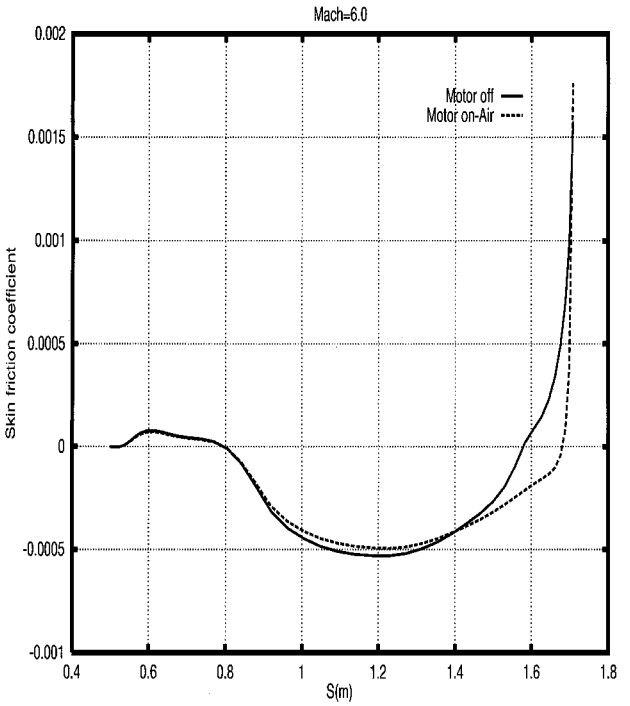

Fig. 19 Comparison of the skin-friction coefficient distributions on the nozzle wall for motor-off and motor-on conditions; Mach = 6.0.

Conclusions

The base flow region of the VEGA K0 lightsat launcher has been investigated for three different freestream Mach numbers. Two different codes have been used in the present work: the CIRA code H2NS, based on a finite volume numerical method on multiblock structured grids, in which the algebraic Baldwin–Lomax turbulence model is employed, and the RAMPANT code, which solves the Reynolds-averaged Navier–Stokes equations on unstructured grids with the two-equation, $\kappa-\epsilon$ turbulence model. Grid independency is attained with both computer codes. A comparison of the results obtained with the two codes at different Mach numbers and both with and without an exhaust plume has been carried out. Even though the overall flowfields do not present remarkable differences, the values of base pressure predicted with RAMPANT are somewhat higher than those obtained with the H2NS code. This can most likely be attributed to the different turbulence models employed.

The influence that different fluid properties (air/combustion gases) and nozzle exit conditions (motor-off/motor-on) have on the base drag has been analyzed. The results show that the fluid characteristics and the presence of the exhaust plume do not modify significantly the flowfield patterns in the base region for the geometry considered in this study.

Acknowledgments

The authors would like to thank M. Amato for his valuable contributions and S. Borrelli and P. Bellomi for many helpful discussions during the course of this work. The RAMPANT code was developed by Fluent, Inc.

References

[1]"Missile Aerodynamics," R-804, AGARD, June 1994.

[2]Moore, F. G., Wilcox, F., and Hymer, T., "Base Drag Prediction on Missile Configurations," *Journal of Spacecraft and Rockets*, Vol. 31, No. 5, 1994, pp. 759–765.

[3]Schiff, L. B., and Sturek, W. B., "Numerical Simulation of Steady Supersonic Flow over an Ogive-Cylinder-Boattail Body," AIAA Paper 80-0066, Jan. 1980.

[4]Deiwert, G. S., "Supersonic Axisymmetric Flow over Boattails Containing a Centered Propulsive Jet," *AIAA Journal*, Vol. 22, No. 10, 1984, pp. 1358–1365.

[5]Ekaterinaris, J. A., "Analysis of Flowfields over Missile Configurations at Subsonic Speeds," *Journal of Spacecraft and Rockets*, Vol. 32, No. 3, 1995, pp. 385–391.

[6]Petrie, H. L., and Walker, B. J., "Comparison of Experiment and Computation for a Missile Base Region Flowfield with a Centered Propulsive Jet," AIAA Paper 85-1618, July 1985.

[7]Childs, R. E., and Caruso, S. C., "On the Accuracy of Turbulent Base Flow Predictions," AIAA Paper 87-1439, June 1987.

[8]Crosicchio, G., and Cramarossa, A., "Vega: A New Low-Cost Approach for a Lightsat Launcher," 46th International Astronautical Congress, International Astronautical Federation, IAF Paper 95-V.1.06, Oslo, Norway, Oct. 1995.

[9]Pandolfi, M., "On the Flux Difference Splitting Formulation," *Notes on Numerical Fluid Mechanics*, 1st ed., Vol. 24, Vieweg, Brunswick, Germany, 1989, pp. 466–481.

[10]Borrelli, S., and Pandolfi, M., "An Upwind Formulation for the Numerical Prediction of Non Equilibrium Hypersonic Flows," *Proceedings of the 12th International Conference on Numerical Methods in Fluid Dynamics* (Oxford, England, UK), edited by J. W. Morton, Springer–Verlag, Berlin, 1990, pp. 416–420.

[11]Borrelli, S., Leone, G., Marini, M., and Schettino, A., "Contributions to Cold and Hot Hyperboloid Flare Problem," Centro Italiano Ricerche Aerospaziali, CIRA-TN-95-0004, Capua, Italy, Oct. 1994; also Fourth European High-Velocity Database Workshop, European Space Agency/European Space Research and Technology Center, Noordwijk, The Netherlands, Nov. 1994.

[12]Serpico, M., Monti, R., and Savino, R., "Heat Flux on Partially Catalytic Surfaces in Hypersonic Flows," *Journal of Spacecraft and Rockets*, Vol. 35, No. 1, 1998, pp. 9–15.

[13]De Filippis, F., Serpico, M., Marini, M., Ravachol, M., and Tribot, J. P., "Comparison Between Numerical and Experimental Results on Different HERMES Elevon Shapes," *Journal of Spacecraft and Rockets*, Vol. 34, No. 3, 1997, pp. 272–278; also AIAA Paper 96-2472, June 1996.

[14]Baldwin, B. S., and Lomax, H.,"Thin-Layer Approximation and Algebraic Model for Separated Turbulent Flows," AIAA Paper 78-257, Jan. 1978.

[15]"RAMPANT 3.1 User's Guide," Fluent, Inc., July 1994.

[16]Sahu, J., "Computations of Supersonic Flow over a Missile Afterbody Containing an Exhaust Jet," *Journal of Spacecraft and Rockets*, Vol. 24, No. 5, 1987, pp. 403–410.

[17]Sahu, J., and Nietubitz, C. J., "Numerical Computation of Base Flow for a Missile in the Presence of a Centered Jet," AIAA Paper 84-0527, Jan. 1984.

[18]Sahu, J., Nietubitz, C. J., and Steger, J. L., "Navier–Stokes Computations of Projectile Base Flow with and Without Mass Injection," *AIAA Journal*, Vol. 23, No. 9, 1985, pp. 1348–1355.

[19]Sahu, J., "Numerical Computations of Supersonic Base Flow with Special Emphasis on Turbulence Modeling," *AIAA Journal*, Vol. 32, No. 7, 1994, pp. 1547–1549.

[20]Sahu, J., "Numerical Investigation of Supersonic Base Flow with Base Bleed," *Journal of Spacecraft and Rockets*, Vol. 34, No. 1, 1997, pp. 62–69.

[21]Falconi, D., "VEGA External Aerodynamic Computation—Input Data Package," Fiat Avio Comprensorio BPD, BPD Internal Document VGA-BPD-SPS-023, Colleferro, Italy, April 1996.

B. A. Bhutta
Associate Editor